New targets and designed inhibitors of ASAP Arf-GAPs derived from structural characterization of the ASAP1/440-kD ankyrin-B interaction

Received for publication, May 9, 2024, and in revised form, August 15, 2024 Published, Papers in Press, September 10, 2024,
https://doi.org/10.1016/j.jbc.2024.107762

Yubing Li[1,2], **Yipeng Zhao**[2,3], **Yaojun He**[1], **Fang Liu**[1], **Lu Xia**[1], **Kai Liu**[2], **Mingjie Zhang**[1,3], **and Keyu Chen**[1,*]

From the [1]Greater Bay Biomedical Innocenter, Shenzhen Bay Laboratory, Shenzhen, China; [2]Division of Life Science, Hong Kong University of Science and Technology, Clear Water Bay, Kowloon, Hong Kong, China; [3]School of Life Sciences, Southern University of Science and Technology, Shenzhen, China

Reviewed by members of the JBC Editorial Board. Edited by Enrique De La Cruz

ASAP1 and its paralog ASAP2 belong to a $PI_{4,5}P_2$-dependent Arf GTPase-activating protein (Arf-GAP) family capable of modulating membrane and cytoskeletal dynamics. ASAPs regulate cell adhesive structures such as invadosomes and focal adhesions during cell attachment and migration. Malfunctioning of ASAP1 has been implicated in the malignant phenotypes of various cancers. Here, we discovered that the SH3 domain of ASAP1 or ASAP2 specifically binds to a 12-residue, positively charged peptide fragment from the 440 kDa giant ankyrin-B, a neuronal axon specific scaffold protein. The high-resolution structure of the ASAP1-SH3 domain in complex with the gAnkB peptide revealed a noncanonical SH3-ligand binding mode with high affinity and specificity. Structural analysis of the complex readily uncovered a consensus ASAP1-SH3 binding motif, which allowed the discovery of a number of previously unknown binding partners of ASAP1-SH3 including Clasp1/Clasp2, ALS2, β-Pix, DAPK3, PHIP, and Limk1. Fittingly, these newly identified ASAP1 binding partners are primarily key modulators of the cytoskeletons. Finally, we designed a cell-penetrating, highly potent ASAP1 SH3 domain binding peptide with a K_d ∼7 nM as a tool for studying the roles of ASAPs in different cellular processes.

Arf GAP with SH3 domain, ankyrin repeat and pleckstrin homology (PH) domain 1 (ASAP1, also known as AMAP1, DDEF1, DEF1, or Centaurin β4) is a $PI_{4,5}P_2$-dependent Arf GTPase-activating protein for Arf1 and Arf5, and is a downstream effector of Arf6 (1–5). Responsible for modulating membrane and cytoskeletal dynamics, ASAP1 plays a crucial role in regulating cell adhesive structures like invadopodia (1, 3–6), podosomes (7–10), and focal adhesions (3, 11, 12), thereby influencing cell attachment and migration (6, 12–15). ASAP1 is highly correlated with malignant phenotypes in various cancers, largely due to its role in modulating cell migration and metastasis (5, 16–23). Studies have shown that overexpression of ASAP1 enhances focal adhesion formation and migration, whereas its loss inhibits podosome and invadopodia formation, and diminishes cell spreading (3, 4, 6). Notably, loss of ASAP1 in transgenic mice led to dysregulated FAK/Src and PI3K/AKT signaling in MEF cells, impairing adipogenic and osteogenic differentiation (24). ASAP1 contains multiple domains, which interact with several key factors at focal adhesions, podosomes, and invadopodia. The N terminal BAR domain of ASAP1 functions in actin bundling, binding to nonmuscle myosin-II and autoinhibition (8, 25); the Arf GTPase domain binds to and activates Arf small GTPases (1–5); the PH domain modulates the ARF-GAP activity (26, 27); the proline rich region interacts with cortactin (17) (though another study showed that cortactin binds to the sequence between the E/DLPPKP repeats and the SH3 domain of ASAP1) (7), CrkL, Src, CD2AP, and Cin85 (4, 7, 17, 28); the SH3 domain of ASAP1 binds to FAK1, PYK2, and paxillin (3, 7, 29–31).

SH3 domains are prevalent protein-protein interaction modules involved in various cellular processes such as intracellular signaling, cytoskeletal rearrangements, and immune responses (32, 33). Human proteome contains around 300 SH3 domains (34–37), they typically recognize proline-rich sequences containing a core "P-X-X-P" sequence element, where "X" represents any amino acid, through defined surface pockets (38–41). However, given that about 25% of human proteins contain proline-rich sequences (32), and most of the known SH3-ligand interactions show relative weak affinities (above micromolar level K_d), predicting highly specific binders of SH3 domains remains challenging.

In this study, we identified strong and specific interactions between the SH3 domains of ASAP1 or ASAP2 and giant ankyrin-B (gAnkB), a large neuronal axon specific scaffold protein. Through structural and biochemical analyses, we unraveled the mechanisms underlying the high affinity and specificity of this binding, leading to the discovery of a consensus sequence motif capable of binding to ASAP1-SH3 with high affinity. A family of previously unknown ASAP1 binding partners was discovered and validated based on this consensus sequence motif. Interestingly, like ASAP1, most of these newly discovered ASAP1 binders are cytoskeleton regulators. The ASAP1 SH3/gAnkB peptide structure allowed us

* For correspondence: Keyu Chen, chenky@szbl.ac.cn.

to design cell-penetrating peptides with exceptionally high affinities in binding to the ASAP1-SH3 domain. We provided proof-of-concept results showing that such cell-penetrating peptides may be used to investigate the cellular functions of ASAPs in the future.

Results

Identification of ASAP1 as a binding partner of gAnkB

The function of ASAP1 has been well established in cancer cells, while its roles in neurons especially in neuronal axons have not been well studied. As a part of our long-term interest in understanding giant ankyrins' function in neuronal axons, we performed screening experiments trying to identify gAnkB-associated axonal proteins. The 440-kD gAnkB is an essential scaffold protein exclusively localized in neuronal axons, regulating axonal plasma membrane and cytoskeletons (42–44). Compared with the ubiquitously localized canonical ankyrin-B splicing isoforms, gAnkB contains a giant axon-specific disordered insertion, contributing to its axon-specific clustering. We used purified recombinant proteins corresponding to different fragments in the neuronal-specific giant insertion as baits for searching binding proteins from mouse brain lysates. In this study, a 250-residue fragment of gAnkB protein (aa. 1476–1727), tagged with three streptavidin-binding peptides (StrepII tags), was used as the bait protein. Several distinct bands of affinity-purified proteins were detected from the SDS-PAGE. Mass spectrometry analysis identified several top-ranked candidates including ASAP1, ASAP2, ANK2, ATP1A2, and ATP1A3 (Fig. 1*A*). Among these, ANK2 (AnkB) should be the bait protein used for the affinity purification. ATP1A2/A3 are also likely nonspecific binders due to their high abundance in brain cells and their frequent recoveries when using other unrelated proteins as baits. ASAP1 and ASAP2 belong to the same family of Arf GTPase-activating proteins and were recovered with very high peptide sequence coverages (Fig. 1*A*). Therefore, we tested the interaction between ASAP1 and gAnkB by performing pull-down experiments using purified 3 × StrepII tagged AnkB protein as the bait and flag-tagged ASAP1 full-length protein expressed in HEK293 cells. As shown in Fig. 1*B*, the interaction between AnkB and the full-length ASAP1 was robustly detected.

SH3 domain of ASAP1 binds to a short fragment of gAnkB

ASAP1 comprises an N terminal BAR domain, a PH domain, an Arf-GAP domain, and three ankyrin-repeats, followed by a C terminal long-disordered region and an SH3 domain (Fig. 1*C*). To confirm the direct binding between ASAP1 and gAnkB and to determine the exact sites on both proteins responsible for the binding, we measured the binding affinity using isothermal titration calorimetry (ITC) with purified proteins. As depicted in Fig. 1, *E* and *F* and summarized in Fig. 1*D*, the SH3 domain (aa. 1083–1147) of ASAP1 binds to gAnkB with a K_d ∼0.19 μM. Neither the proline-rich region (aa. 732–915) nor the "E/DLPPKP"-repeat sequence (aa. 903–1082) displayed any interaction with gAnkB. Therefore, the ASAP1 SH3 domain is responsible for binding to gAnkB. Similarly, to locate the ASAP1 SH3 binding sites on the gAnkB, we truncated the gAnkB bait fragment (aa. 1477–1792) into shorter segments and determined their affinities with ASAP1 SH3 by ITC. As summarized in Fig. 1*D*, the shortest sequence capable of binding ASAP1 was mapped to a 12-residue fragment of gAnkB (aa. 1699–1710). This short peptide is highly conserved in vertebrate gAnkB (Fig. S1*A*), but does not exist in gAnkB's paralog ankyrin-G or ankyrin-R, suggesting that ASAP1 is a specific gAnkB binder in animal brains. We further note that the binding between ASAP1 and gAnkB is the strongest interaction among all reported ASAP1-SH3 binding proteins (45). In addition, strong binding between the SH3 domain of ASAP2, a homolog of ASAP1 that is also identified in our AP-Mass, and gAnkB is also detected by ITC (K_d ∼68 nM; Fig. S1*B*). In the subsequent study, we focused on ASAP1 to study its interaction with gAnkB and the derived conclusions should be applicable to ASAP2 as well.

Crystal structure of the ASAP1-SH3/AnkB complex reveals a new SH3 target binding mode

The binding of SH3 domains to their ligand peptides typically involves a minimal "P-X-X-P" motif. Curiously, the ASAP1 SH3 binding peptide from gAnkB contains only one proline residue, and yet the peptide binds to the SH3 domain with an affinity (K_d ∼0.19 μM) stronger than most of the reported SH3/target interactions. To elucidate the mechanism underlying the observed strong interaction between ASAP1 and gAnkB, we determined the crystal structure of ASAP1-SH3 in complex with the gAnkB peptide at the atomic resolution of 2.07 Å (Fig. 2, *A* and *B*, Table 1).

In the complex structure, ASAP1-SH3 adopts the typical five-stranded SH3 fold. The ASAP1-SH3 also contains two SH3 domain-defining pockets (pockets I & II) responsible for binding two proline residues in the canonical "P-X-X-P" motif (Fig. 2, *A* and *C*) (40). In our structure, pocket I interacts with the hydrophobic Ile instead of Pro at the 0 position and pocket II accommodates Pro at the +3 position (Figs. 2*A*, 4*A*) from the gAnkB peptide. Prominently, ASAP1-SH3 contains two highly negatively charged pockets (pockets III and IV), with pocket III interacting with Lys at the +2 position and pocket IV accommodating Arg at the +5 position of the gAnkB peptide (Figs. 2*A* and *D*, 4*A*). Most uniquely, ASAP1-SH3 contains a large and flat negatively charged surface that interacts electrostatically with Arg at the +6 position and likely also with Lys at the +7 position (Figs. 2*A*, S1, *D* and *E*). These charge-charge interactions in three regions outside the pockets I and II underlie the strong and specific interaction between gAnkB and ASAP1-SH3.

To validate our structural model, key residues in the gAnkB peptide were mutated to assess their effects on the binding to ASAP1-SH3. As summarized in Fig. 2*E*, mutation of K1702 at the +3 position to Glu weakened the interaction by ∼264-fold; reversing the charge of R1705 at the +6 position by Glu also

A

Coverage (%)	Area	#Peptides	Avg. Mass	Candidate
67	1.08E+09	84	127421	ASAP1
59	4.29E+08	62	106805	ASAP2
2	3.31E+07	8	426265	ANK2
14	2.05E+06	12	112217	ATP1A2
12	1.25E+06	10	111691	ATP1A3

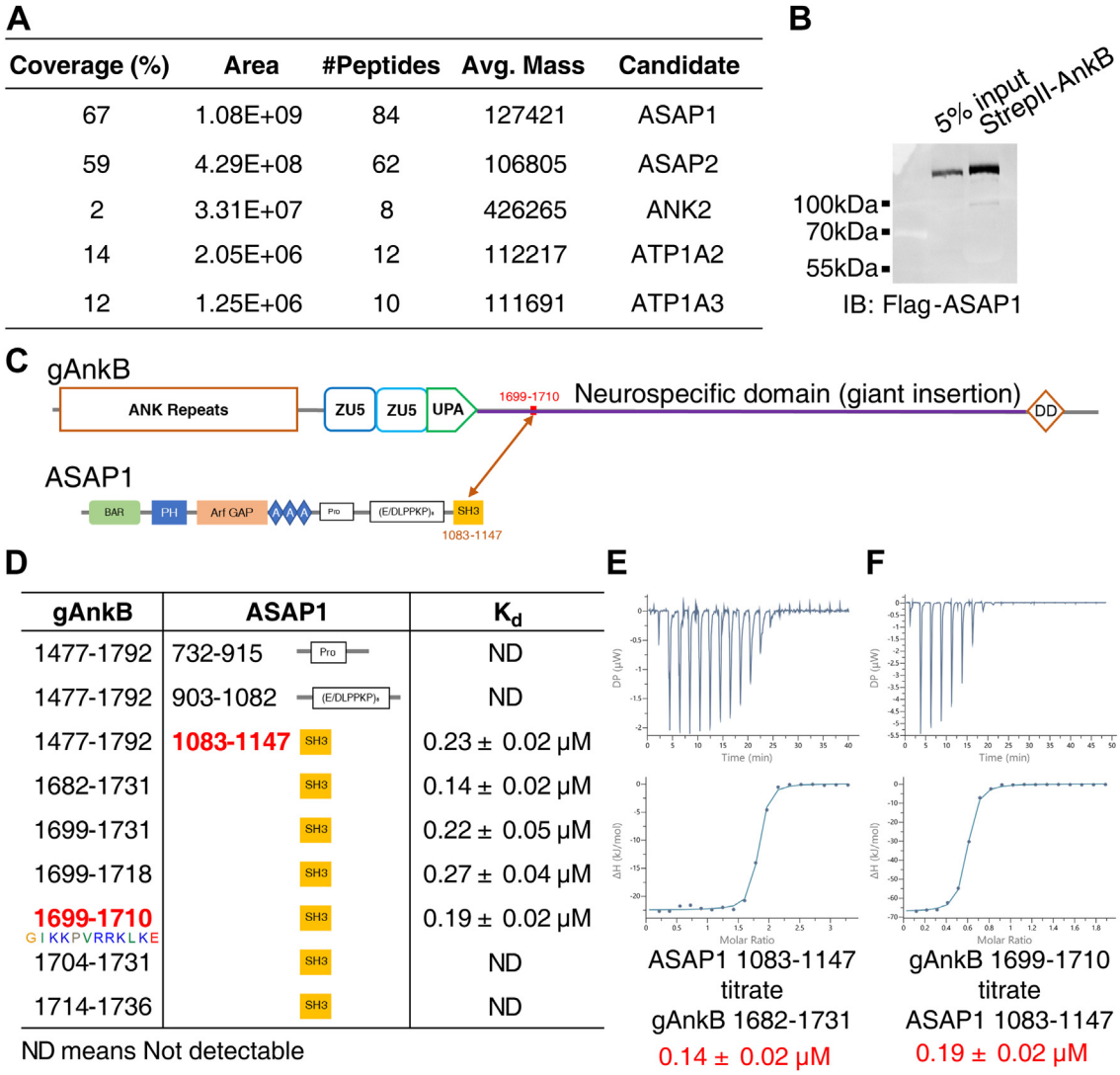

Figure 1. Identification and binding-site mapping of ASAP1-gAnkB interaction. *A*, list of the top-ranked proteins identified by the affinity purification and mass spectrum. "Coverage%" means the percentage of protein sequences that can be covered by all the identified peptides; "Area" means the highest peak intensity of the mass spectrum peak corresponding to the peptide segment; "#Peptides" means the total number of peptides contained in the identified protein; "Avg. Mass" means the average molecular weight of the protein. *B*, pull-down assay of the binding between purified gAnkB (aa. 1476–1727) to Flag-tagged full-length ASAP1 expressed in HEK293T cells. IB, immunoblot. *C*, domain organizations of human 440-kD gAnkB and ASAP1. The minimal binding regions from the two proteins revealed from experiments in panel D are indicated by an *arrow*. *D*, affinity directed binding site mapping of the interaction between gAnkB and ASAP1. Protein boundaries for each ITC-based binding reaction and derived dissociate coefficients are listed. Numbers labeled in *red* mean these are the shortest fragments in each protein that possess the full binding capability. *E*, raw ITC curve showing ASAP1-SH3 binds to gAnkB (aa. 1682–1731) with ∼0.14 μM binding affinity. *F*, raw ITC curve showing ASAP1-SH3 binds to a 12-residue peptide derived from gAnkB (aa. 1699–1710) with ∼0.19 μM binding affinity. gAnkB, giant ankyrin-B; ITC, isothermal titration calorimetry.

weakened the interaction by ∼105-fold; a double mutation by replacing K1702 and R1705 with Glu completely abolished the interactions. These results support that the charge-charge interactions are critical for the binding of ASAP1 SH3 to the gAnkB peptide. Surprisingly, mutation of P1703 at the +3 position by a flexible Gly decreased the binding affinity by only ∼3-fold, indicating the sole Pro residue in the gAnkB peptide plays a minor role in the ASAP1 SH3 binding. Taken together, the above structural and biochemical studies reveal that the ASAP1 SH3 domain recognizes gAnkB chiefly *via* extensive charge-charge interactions instead of the canonical "P-X-X-P" motif-based bindings. The defining Pro residues are not essentially for ASAP1 SH3 ligand peptides.

Mechanisms underlie the high affinity and specificity of the ASAP1-SH3/gAnkB interaction

To elucidate the mechanism underlying the high affinity and the unique interaction between ASAP1-SH3 and gAnkB, we compared our structure with previously reported ASAP1-SH3/APC (Protein Data Bank (PDB): 2rqu) (46) and ASAP1-SH3/MICAL1 (PDB: 8hlo) (45) structures. Similar to the ASAP1-SH3/MICAL1 and ASAP1-SH3/APC structures, ASAP1-SH3 contains two additional highly negatively charged pockets (pockets III and IV) for incorporating the conserved lysine residue at the +2 position and arginine residue at the +5 position, in addition to the two SH3 domain signature pockets (pockets I and II) (Fig. 3, *A* and *B*). Substantial differences in

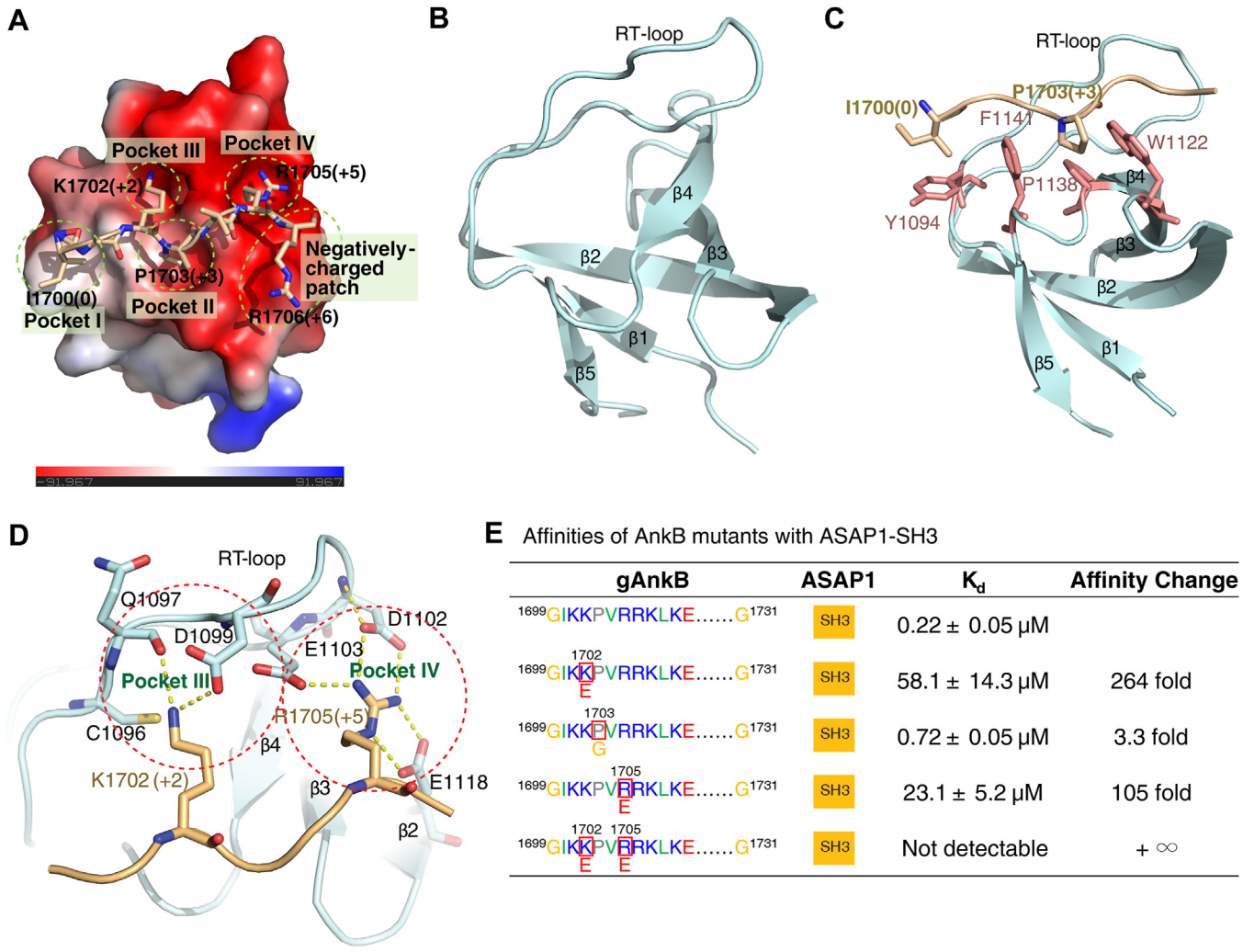

Figure 2. Four binding pockets and a negative-charged surface patch are identified from the gAnkB/ASAP1-SH3 crystal structure. *A*, structure of ASAP1-SH3 in complex with the gAnkB peptide. ASAP1-SH3 is shown in the surface charge potential model and the gAnkB peptide is shown in the *stick* model. Four identified binding pockets on SH3 for AnkB binding are circled by *green dashed lines*, labeled as Pocket I ∼ IV, respectively. A highly negatively charged surface patch on SH3 is also circled by a *green dashed line*. Numbers within the brackets indicate the designated position of amino acid residue on gAnkB (Fig. 4*A* for detailed positions). *B*, ribbon diagram of the ASAP1-SH3 domain in complex with gAnkB are depicted in an identical orientation as the surface model in panel A for locating key gAnkB binding elements from the SH3 domain (Fig. 3*C* for detailed positions of amino acid residues in this domain). *C*, ribbon diagram combined with the stick model showing the interact residues in pockets I and II in the complex. *D*, stick model showing the charge-charge interactions between ASAP1-SH3 and the gAnkB peptide in pockets III and IV (Figs. 3*C* and 4*A* for detailed positions of amino acid residues). *E*, affinities of the gAnkB peptide mutants binding to ASAP1-SH3 determined by ITC. gAnkB, giant ankyrin-B; ITC, isothermal titration calorimetry.

their binding mode also exist. Instead of a proline residue of the canonical "P-X-X-P" motif in MICAL1 or APC (SAMP repeat 1 sequence), a highly conserved Ile at the 0 position in gAnkB is responsible for interacting with pocket 1 in ASAP1-SH3 (Figs. 2*A*, 3*B* and 4*A*). MICAL1 completely lacks the positively charged residues at the +6 and + 7 positions to interact with a negatively charged flat surface unique to ASAP1-SH3 (Figs. 3*B* and 4*A*), explaining the weaker binding affinity of MICAL1 to ASAP1. APC has only one positively charged Lys at the +6 position, and this Lys partially occupies the negatively charged flat surface of ASAP1-SH3 and the rest of the APC peptide turns away from the charged surface (Figs. 3*B* and 4*A*), again providing an explanation to the weaker binding of APC to ASAP1 (45). Interestingly, the residue at the +3 position of APC is a Ser instead of Pro and this Ser residue can also occupy pocket II of ASAP1-SH3 (Fig. 3, *A* and *B*), consistent with our result showing that the Pro at the +3 position in gAnkB peptide is not essential for the ASAP1 binding (Fig. 2*E*). In summary, the gAnkB peptide make full use of all binding sites (pockets I ∼ IV and the flat negatively charged surface) on ASAP1-SH3 domain and thus binds to ASAP1 with a high affinity.

Similar to what was revealed by Jia *et al.* (45), a unique "C-X-X-(D/E)" sequence in the R/T-loop of ASAP1-SH3 creates a negatively charged binding pocket (pocket III) for the lysine residue at position +2 of the gAnkB peptide. This "C-X-X-(D/E)" sequence is present in ASAP1, ASAP2, GRAF1, GRAF2, GRAF3, and SKAP1, but not in the SH3 domains of other proteins. Comparing the sequences of the SH3 domains in these proteins revealed a series of residues in ASAP1-SH3 essential for gAnkB binding but partially or totally missing in GRAF1, GRAF2, GRAF3, or SKAP1 (Fig. 3*C*). The aspartic acid D1102

Table 1
Crystallographic data collection and refinement statistics

Data collection	ASAP1/AnkB
Space group	P 1
Wavelength (Å)	0.979183
Unit cell parameters	
a, b, c (Å)	39.9225, 52.0739, 56.9089
α, β, γ (°)	111.416, 90.1631, 112.462
Resolution range (Å)	32.49–2.07 (2.12–2.07)
No. of unique reflections	23,173 (1695)
Redundancy	3.2 (2.8)
I/σ	8.1 (5.7)
Completeness (%)	97.6 (95.4)
R_{merge}[a](%)	12.1 (21.3)
$CC_{1/2}$[b]	0.941 (0.674)
Structure refinement	
Resolution (Å)	2.07
R_{work}[c](%)	18.49 (19.80)
R_{free}[d](%)	22.47 (26.28)
Root-mean-square deviation	
Bonds (Å)	0.009
Angles (°)	1.559
Average B factor (Å^2)	17.37
No. of atoms	
Protein	4425
Water	313
Other molecules	1
No. of reflections	
Working set	23,129
Test set	1131
Ramachandran plot (%)	
Favored	99.22
Allowed	0.78
Outliers	0.00

Numbers in parentheses represent the values for the highest resolution shell.
[a] $R_{merge} = \Sigma|I_i - <I>|/\Sigma I_i$, where I_i is the intensity of measured reflection and $< I >$ is the mean intensity of all symmetry-related reflections.
[b] $CC_{1/2}$ was defined in Karplus and Diederichs (2012).
[c] $R_{work} = \Sigma_W||F_{calc}| - |F_{obs}||/\Sigma|F_{obs}|$, where F_{obs} and F_{calc} are observed and calculated structure factors. W is working dataset of about 95% of the total unique reflections randomly chosen and used for refinement.
[d] $R_{Free} = \Sigma_T||F_{calc}| - |F_{obs}||/\Sigma|F_{obs}|$, where T is a test dataset of about 5% of the total unique reflections randomly chosen and set aside prior to refinement.

in the R/T-loop is in pocket IV and critical for binding to Arg (+5 position, Fig. 4*A*). This residue is missing in the GRAF family proteins (Fig. 3*C*). E1118 of ASAP1 at the end of the β2 strand also forms part of the pocket IV (Fig. 4*A*). This residue is missing in SKAP1 and the GRAF family SH3 domains (Fig. 3*C*). Finally, D1119 and E1121 of ASAP1, located in the loop between β2 and β3, together form the negatively charged flat surface patch interacting with the positively charged residue at the +6 and + 7 positions of gAnkB. These two negatively charged residues are partially or totally missing in SKAP1 and the GRAF family SH3 domains (Fig. 3*C*). Taken together, the above structure-based amino acid sequence analysis uncovers the molecular basis underlying the highly specific target recognition mechanism by the ASAP1/2 SH3 domains.

Consensus sequence motif of ASAP1-SH3 binders and identification of new high-affinity ASAP1 binding partners

Based on the analysis presented above, a consensus binding motif can be deduced as peptide ligands that may bind to the ASAP1-SH3 domain with high affinity and specificity. The motif can be summarized as Φ-[K/R]-K-P-{P/G/S}-R-[K/R]-{D/E}, as illustrated in Fig. 4*B*. Here, Φ at position 0 denotes hydrophobic residues, together with proline at position +3, contributing hydrophobic packing forces to pocket I and II respectively; [KR] at +6 position represents positively charged lysine or arginine residues for binding negatively charged patch; [KR] at +1 position is highly conserved in gAnkB and other ASAP1-SH3 binders;{P/G/S} in curly brackets indicates that this position should not be Pro, Gly, or Ser, to avoid their potential influence on the backbone freedom; R at position +5 is responsible for interacting with pocket IV; {D/E} in curly brackets means that negatively charged residues are not well-tolerated at this position due to the negatively charged surface patch of the SH3 domain. We searched the SWISSPROT protein sequence database to identify potential ASAP1-SH3 binding proteins. A total of 20 proteins containing such sequence motifs were found in the human and mouse proteomes (Table S1). Among these 20 proteins, we further narrowed down the ones that contain evolutionarily conserved predicted ASAP1 SH3 binding motifs for further validation. We discovered that proteins including Clasp1, Limk1, and ALS2 exhibited specific binding to the ASAP1-SH3 domain (Fig. 4, *C* and *D*). In addition, an additional search for proteins containing the imperfect [K/R]-K-P-{P/G/S}-R-[K/R]-{D/E} motifs recovered 53 human or mouse proteins as potential ASAP1 SH3 binders (Table S2). We picked DAPK3, ARHGEF7 (β-Pix), and PHIP among this list of proteins, again because the identified sequence motif in each of these proteins is evolutionally conserved. Satisfyingly, peptide fragments containing the identified sequence motif derived from DAPK3, ARHGEF7 (β-Pix), and PHIP withal bind to ASAP1-SH3 with submicromolar K_d values (Fig. 4, *C* and *E*). Pull-down assays using the full-length proteins further confirmed their interactions with ASAP1-SH3 (Fig. S2). It is noted that the residue at the 0 position of the ASAP1-SH3 binding motif from DAPK3, ARHGEF7 (β-Pix), and PHIP is neither a Pro nor a hydrophobic residue, further indicating that the canonical pocket I and pocket II binding Pro residues (*i.e.*, the Pro residues in the canonical "PXXP" motif) are not essential for the ASAP1-SH3 binding ligands. In contrast, the negatively charged pocket III, pocket IV, and the negatively charged flat surface illustrated in Fig. 2*A* are more critical in defining the cognitive ligands for the ASAP1 SH3 domain.

Notably, many of the newly identified binding partners, for example, Limk1, are associated with the cytoskeleton remodeling function of ASAP1. Limk1 serves as an upstream regulator that phosphorylates cofilin to regulate actin polymerization in many biological processes. Similar to the known ASAP1-SH3 domain binding kinases FAK1 and PYK2, Limk1 plays significant roles in the functions of invadosomes (3, 30, 47, 48), fitting with reported ASAP1's roles in invadosomes. In our preliminary *in vitro* test using recombinant Limk1 kinase protein, we unexpectedly found that the ATP consumption was greatly promoted upon the addition of ASAP1-SH3 to the Limk1 solution, and such ATP hydrolysis is ASAP1-SH3 dose-dependent (Fig. 4*F*). Further *in vitro* Limk1 phosphorylation assay using a pan phospho-tyrosine antibody (CST, Cat. 8954S, lot: 8) to detect the phosphorylated proteins was conducted, and myelin basic protein (MBP) was used as a model substrate of Limk1 in the assay (49). As demonstrated in Fig. S3, *A*, *B* and *D*, SH3 can be phosphorylated by Limk1 in a

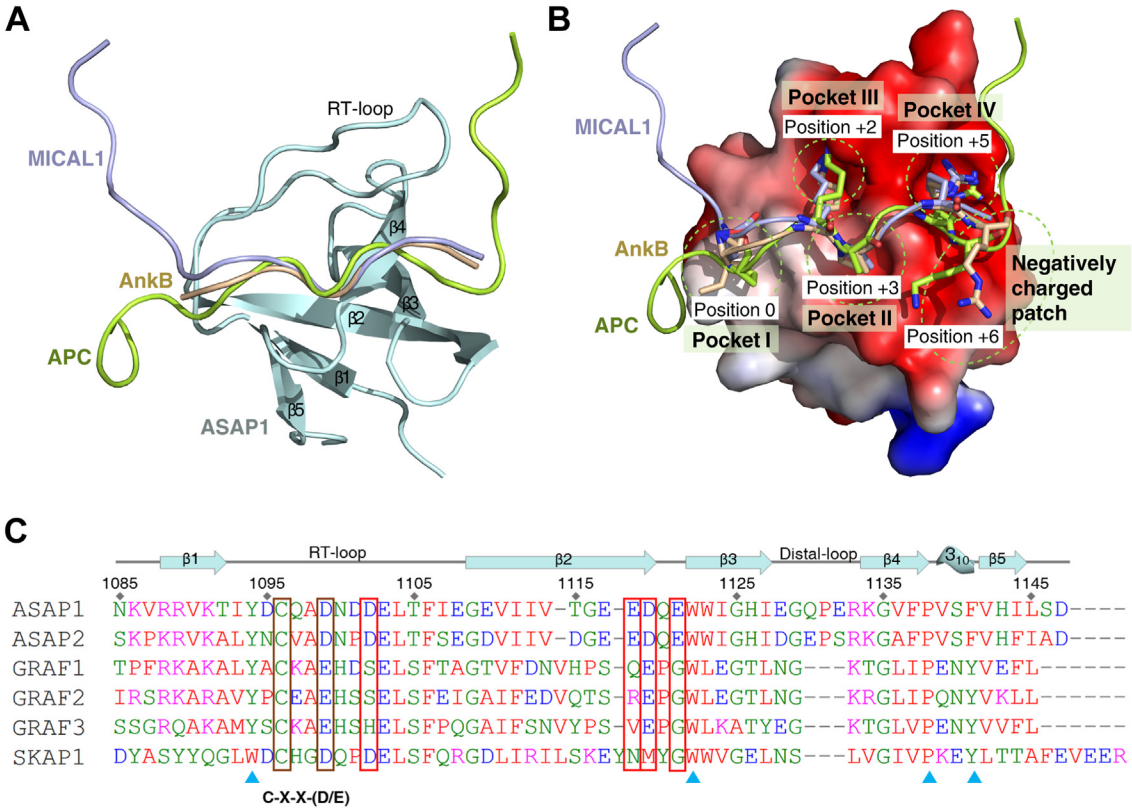

Figure 3. Mechanisms underlying the high affinity binding between ASAP1-SH3 and gAnkB. *A*, the ASAP1-SH3/gAnkB structure is aligned with the ASAP1-SH3/APC (PDB: 2rqu) and ASAP1-SH3/MICAL1 (PDB: 8hlo) structures. As SH3 domains from these structures are almost identical, for simplicity, only the SH3 from the ASAP1-SH3/gAnkB structure is shown. *B*, surface charge potential model combined with the stick model showing the bindings of the gAnkB, APC, and MICAL1 peptides to ASAP1-SH3. The side chains of the residues from the peptide ligands binding to pockets I ∼ IV are drawn in the stick model. *C*, sequence alignment of six SH3 domains that contain the "C-X-X-D/E" motif in the RT-loop. Negatively charged residues in ASAP1-SH3 that are essential for binding to gAnkB are boxed in *red*. Key residues forming the pocket I and II are pointed by *blue triangles* (Fig. 2*C* for their positions on the structure). gAnkB, giant ankyrin-B; PDB, Protein Data Bank.

time-dependent and dose-dependent manner. Notably, our results indicate that the Limk1 kinase domain can phosphorylate itself *in vitro* (Fig. S3, *E* and *F*). Additionally, SH3 was found to inhibit this autophosphorylation process (Fig. S3, *A*, *C* and *D*). Surprisingly, the inclusion of SH3 in the reaction system appeared to enhance Limk1 kinase activity, as evidenced by the increased phosphorylation of MBP or SH3 (Fig. S3, *A* and *C*). This effect may be attributed to the inhibition of Limk1 autophosphorylation by SH3, which in turn activates the kinase activity. More in-depth studies should be conducted in the future to confirm the existence of this phenomenon in living cells and to delineate the precise underlying mechanism.

Designed cell penetrating super strong ASAP1-SH3 binding peptides

Given the ability of ASAP1-SH3 to bind to many proteins involved in various biological processes, understanding the mechanisms of ASAP1 in living cells are challenging. Here, we aimed to develop a potent inhibitory peptide capable of effectively blocking the bindings of ASAP1/ASAP2's SH3 domains to all of its binding target proteins. Five peptides were designed and assessed with the results depicted in Fig. 5*A*. Peptide 1 (P1), a chimera of APC and gAnkB, displayed a higher affinity (K_d = 64.0 ± 7.1 nM) for ASAP1-SH3 compared to the individual APC or gAnkB peptides. Peptide 2 (P2), which substituted proline at position 0 of the motif with isoleucine, did not enhance affinity. Peptide 3 (P3), where glutamic acid at position +10 was changed to arginine, showed no improvement in affinity. Peptide 4 (P4), a chimera of MICAL1 and gAnkB, exhibited a similar affinity (K_d = 66.2 ± 11.1 nM) to P1. Remarkably, peptide 5 (P5) demonstrated an exceptionally strong binding affinity for ASAP1-SH3 (K_d ∼7.0 nM, Fig. S4*A*) and ASAP2-SH3 (K_d ∼27.1 nM, Fig. S4*B*), as well as potent ability to inhibit ASAP1-SH3 from binding to its partners (Fig. S4*C*). P5 was specifically designed based on the solved gAnkB/ASAP1-SH3 structure, with the addition of proline and isoleucine at the -1 and -2 positions, respectively, to enhance hydrophobic interactions with the hydrophobic surface peripheral to pocket I on SH3, and the inclusion of a positively charged "KRR" sequence at positions -3 to -5 to facilitate charge-charge interactions with the negatively charged surfaces on SH3 (see predicted structure of the P5/SH3 complex by AlphaFold3; https://alphafoldserver.com, Fig. S4*D*). To test the specificity of P5 toward different SH3 domains, five representative SH3 domains from various

A

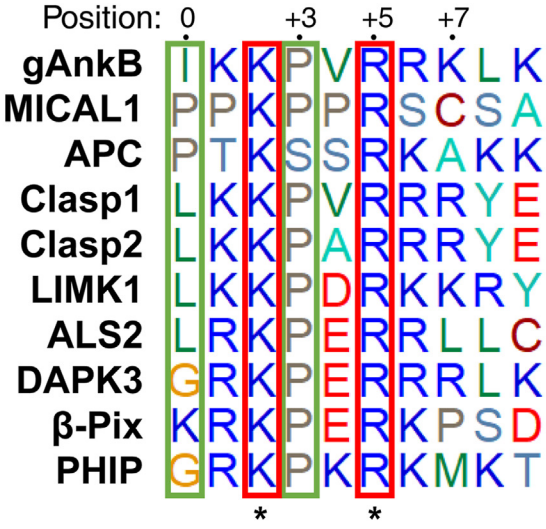

B

C

Candidate	Binding affinity [K_d]
ALS2	11.1 ± 2.6 μM
Clasp1	8.9 ± 1.0 μM
DAPK3	767.0 ± 45.9 nM
LIMK1	555.0 ± 79.8 nM
ARHGEF7/β-Pix	820.0 ± 45.8 nM
PHIP	119.0 ± 21.4 nM

D

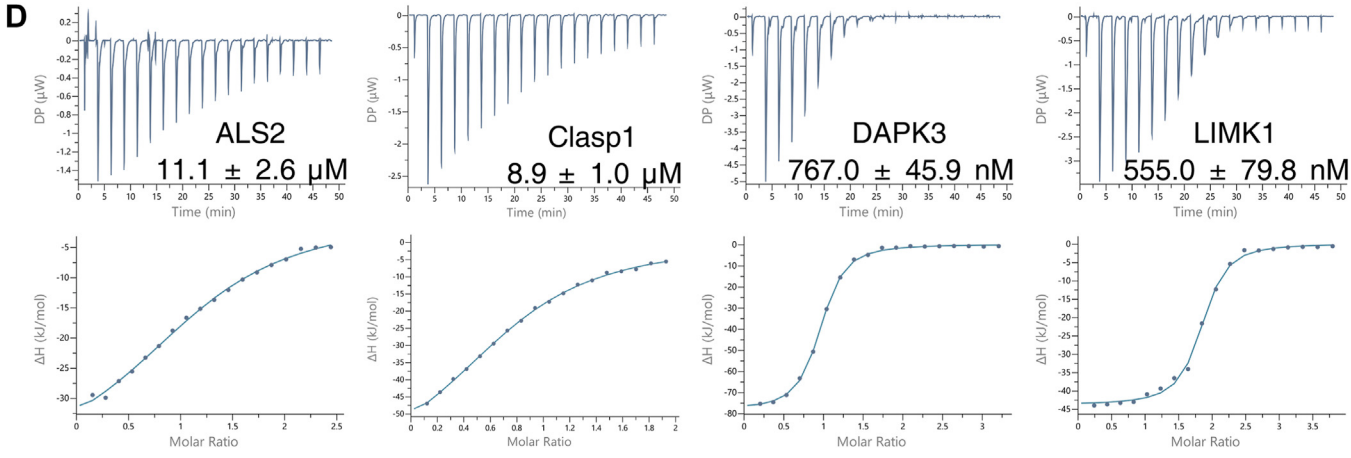

E

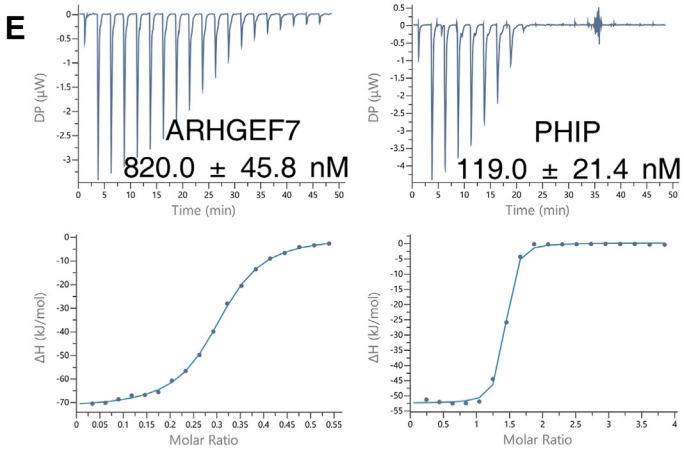

F

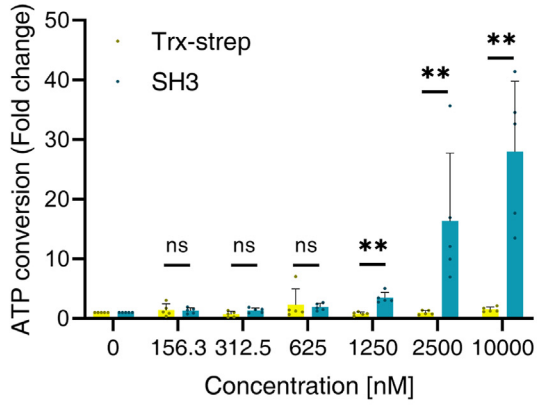

Figure 4. Consensus sequence motif and newly identified ASAP1-SH3 binding partners. *A*, sequence alignment of the known (MICAL1 and APC) and newly identified ASAP1-SH3 binding ligand peptides. For APC, its first SAMP repeating sequence region was shown. Arbitrarily assigned positions of the motif are displayed on the top. *B*, consensus sequence motif of ASAP1-SH3 binders. Φ represents hydrophobic residues; [K/R] means either lysine or arginine; {P/G/S} means any amino acid except for proline, glycine, and serine; {D/E} means any amino acid except for negatively charged residues. Arbitrarily assigned positions of the motif are displayed on the top. *C*, summary of the newly discovered ASAP1-SH3 binding partners with corresponding binding dissociation coefficient determined by ITC. *D*, Raw ITC curves showing the bindings of newly discovered peptides derived from ALS2, CLASP1, DAPK3, and LIMK1 to ASAP1-SH3. *E*, Raw ITC curves showing the bindings of newly discovered peptides derived from ARHGEF7 and PHIP to ASAP1-SH3. *F*, quantification of the LIMK1 kinase phosphorylation assays with indicated concentrations of ASAP1-SH3 and Trx-strep (control). The *Y*-axis shows the ATP conversion rate (Fold change compared to the control group that without adding ASAP1-SH3 or Trx-strep). $^{**}p = 0.0079$ was calculated using the Mann-Whitney test for concentration higher or equal to 1250 nM and data were shown as mean ± SD (n = 5, from three different experiments). ns, not significant. ITC, isothermal titration calorimetry.

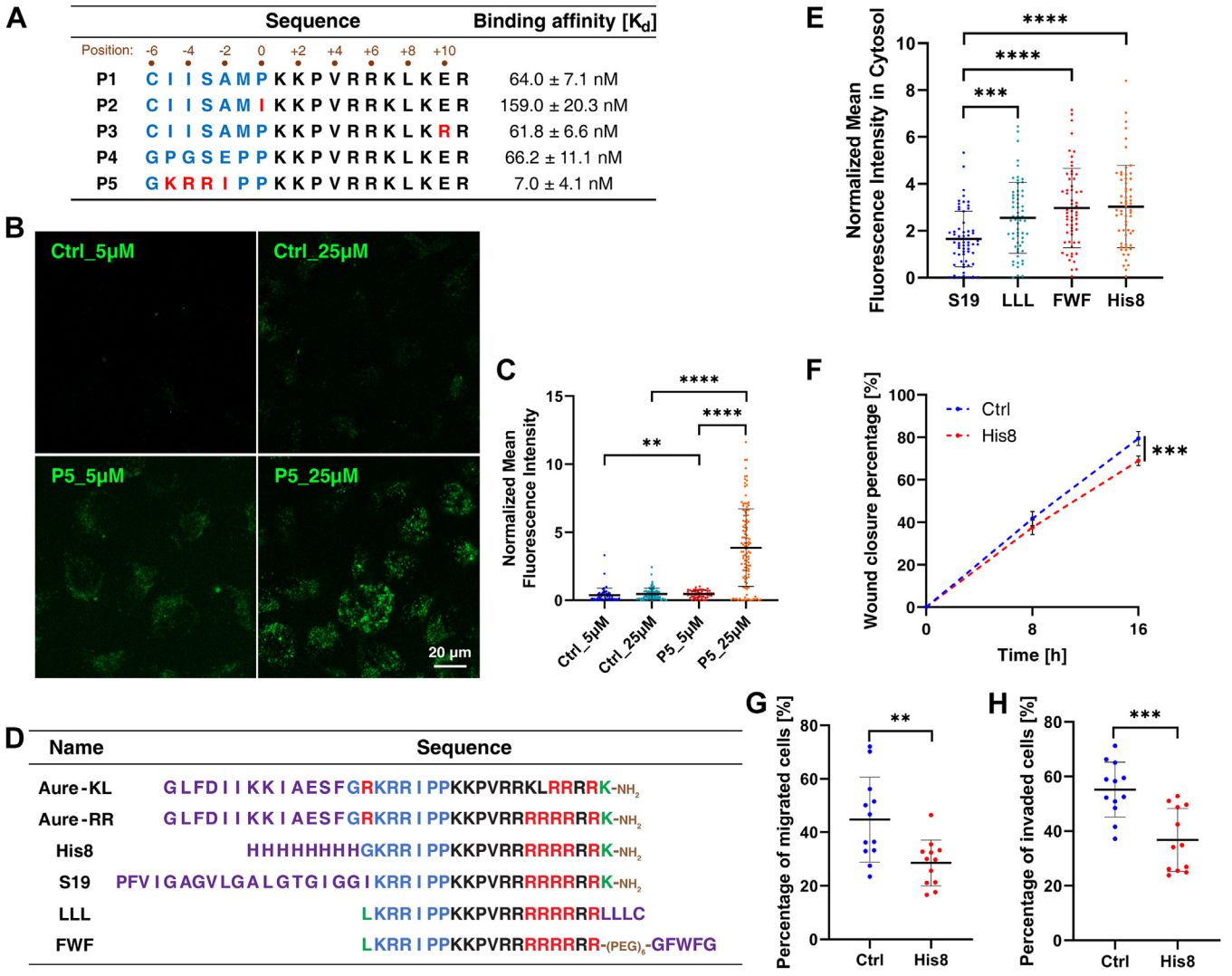

Figure 5. Designed peptides blocking ASAP1-SH3 and modifications to promote cell-penetrating activity of the peptide. *A*, summary of the sequence and binding affinity of the designed peptides for blocking ASAP1-SH3. *Black* residues derived from gAnkB. *Blue* residues derived from APC or MICAL1. *Red* residues represent designed mutations. *B*, representative fluorescence images of HeLa cells treated with indicated concentrations of FITC labeled scrambled control (Ctrl) peptide or P5 peptide with P5 exhibiting strong cell-penetrating ability. The scale bar represents 20 μm. *C*, quantification of normalized mean fluorescence intensity of cells treated with indicated concentrations of scrambled control or P5 peptides for 24 h. Data are mean ± SD of three independent experiments with n = 56 cells for 5 μM and n = 118 cells for 25 μM. $^{**}p = 0.0025$, $^{****}p < 0.0001$; the two-tailed unpaired Student's *t* test was used to compare P5_5 μM *versus* P5_25 μM. The Mann-Whitney test was used to compare Ctrl_5 μM *versus* P5_5 μM and Ctrl_25 μM *versus* P5_25 μM. *D*, sequence alignment of the modified P5 peptides for promoting the endosome escaping. Residues shown in *purple* are designed elements to promote endosome escaping. The *red-colored* "R" represents additional arginine residues added to the P5 peptide for promoting cell penetrating ability. The *green-colored* residues are positions where FITC fluorophore is labeled. "-NH2" means the carboxyl end of the peptide is amidated to neutralize the negative charge. $(PEG)_6$ in FWF peptide represents a spacing linker that is composed of six consecutive ethylene glycol molecules. *E*, quantification of normalized mean fluorescence intensity in the cytosol of cells treated with 10 μM of S19, LLL, FWF, or His8 peptides for 24 h. Data are mean ± SD of three independent experiments with n = 60 cells. $^{***}p = 0.0006$, $^{****}p < 0.0001$; as determined by the Mann-Whitney test. *F*, quantified wound closure percentage of HeLa cells pretreated with 40 μM His8 or Ctrl peptides at different time points. Data are mean ± SD of five independent experiments. $^{***}p = 0.0009$; as determined by the two-tailed unpaired Student's *t* test. Representative images are shown in Fig. S5*H*. *G*, quantified percentage of migrated cells pretreated with 40 μM Ctrl or His8 peptides in the nonmatrigel-coated (uncoated) chamber in the transwell assay. Data are mean ± SD of three independent experiments with n = 12 random fields. $^{**}p = 0.0051$; as determined by the two-tailed unpaired Student's *t* test. Representative images are shown in Fig. S5*I*. *H*, quantified percentage of invaded cells pretreated with 40 μM Ctrl or His8 peptides in matrigel-coated chamber in the transwell assay. Data are mean ± SD of three independent experiments with n = 12 random fields. $^{***}p = 0.0004$; as determined by the two-tailed unpaired Student's *t* test. Representative images are shown in Fig. S5*J*. gAnkB, giant ankyrin-B.

proteins, each involved in unique biological processes related to cellular functions of podosomes/invadosomes, were selected to examine their interaction with P5 (50–54). Each of these five SH3 domains represents a member of divergent SH3 subtypes, as defined by their structural and functional characteristics (for details, see References (55, 56)). Remarkably, our ITC experiments revealed that none of these SH3 domains showed detectable bindings to P5 (Fig. S4, *E–I*). Notedly, one of these five SH3 is from SKAP1, which exhibits a high degree of sequence similarity with ASAP1-SH3 (Fig. 3*C*), and belongs to the same subgroup as ASAP1-SH3. These experiments support our conclusion that the P5 peptide has high specificity in binding to ASAP1/2 SH3 domain.

The P5 peptide is short, highly positive charged, and with several hydrophobic residues, which are hallmarks of certain cell-penetrating peptides reported in the literatures (57). Indeed, P5 displayed efficient cell penetration, and a control peptide with a scrambled sequence of P5 showed low cell penetration activity (Fig. 5, *B* and *C*). However, a substantial portion of the internalized peptides became trapped in endosomes (Fig. 5*B*), a common limitation known for many cell-penetrating peptides and hindering their applications (57, 58). To promote endosome escaping of P5, various strategies were explored by incorporating additional endosome-escaping moieties (58–61) into the peptide as depicted in Fig. 5*D*. Among the modified P5 peptides, Aure-KL and Aure-RR were deemed too toxic for cells (Fig. S4*J*). Both FWF and His8 peptides demonstrated efficient cell penetration and better endosome escaping abilities, whereas S19 and LLL exhibited weaker effects on endosome escape, despite retaining good cell-penetrating abilities (Figs. 5*E*, S4*K*). Subsequently, before His8 was selected to evaluate its impact on HeLa cell migration and metastasis through wound healing and transwell assays, we confirmed His8's high affinity (Fig. S5, *A* and *B*) and high selectivity toward ASAP1/2-SH3 (Fig. S5, *C*–*G*), indicating that modifications on P5 did not perturb its interactions with ASAP1/2. As illustrated in Fig. 5, *F*–*H* (Fig. S5, *H*–*J* for representative images), the His8 cell-penetrating peptide reduced migration, speed, and metastatic activity in HeLa cells. Our control experiments confirmed that these phenotypes are not due to altered cell proliferation (Fig. S5*K*) or certain nonspecific effects of the peptide loaded to the cells (Fig. S6). In short, this result provides proof-of-concept evidence showing the use of the His8 peptide in manipulating ASAP1/2 function in cells.

Discussion

New binding partners of ASAP1 and cell penetrating SH3-blocking peptides

SH3 domains usually exhibit binding affinities above the micromolar range, lacking high specificity. However, our current study unveiled a robust and specific interaction between the SH3 domain of ASAP1 and a unique short peptide fragment from gAnkB, characterized by a K_d value of 0.19 ± 0.02 μM. Structural and biochemical analyses of this interaction identified a consensus sequence motif for predicting high-affinity binders of ASAP1-SH3, leading to the discovery of many previously unrecognized ASAP1 binders. All predicted binders, Clasp1, β-Pix, DAPK3, PHIP, and Limk1 to ASAP1-SH3, were tested positive in binding to ASAP1-SH3, and most of them with submicromolar binding affinities. These newly discovered ASAP1 binders as well as previously identified ASAP1-SH3 binding proteins such as APC, MICAL1, FAK1, and PYK2 are all known cytoskeleton modulators, suggesting a general role of ASAPs in cytoskeleton regulation.

ASAP1 and ASAP2 share high structural and sequence similarities, thus functional redundancy of these two paralogs may exist and thereby complicate their functional studies in living cells. Both of their SH3 domains could potentially interact with many proteins, underscoring the necessity of a genetically encodable blocking peptide to simultaneously block the SH3 domain of ASAPs and effectively modulate ASAP1/2's function in living cells. Our design of a super high-affinity binding peptide for ASAP1-SH3 with a K_d ∼7 nM, which is tenfold stronger than the known strongest natural binding proteins of ASAP1-SH3, represents a significant advancement. To the best of our knowledge, this binding interaction represents one of the strongest SH3-ligand interactions identified in the proteome to date (Table S3) (62–68). Additionally, the robust cell-penetrating abilities of this peptide should facilitate the use of the peptide (derivatives to be developed in the future) for cellular manipulations of ASAPs.

ASAP1 may function in neuron axons to regulate cytoskeletons

Cytoskeletons are tightly regulated due to the demanding functions and the extreme morphologies of neuronal axons (69–71). gAnkB, a high-risk factor for autism spectrum disorders (43, 72, 73), exclusively localizes to axons and is essential for axon development. We and others showed that gAnkB is a potent inhibitor of stochastic collateral axon branching by its ability to regulate microtubule dynamics and coupling microtubules with axonal plasma membranes, defects in which contributes to the formation of aberrant neuronal connections manifested in the autism models of rodents (43, 44). Similarly, ASAP1 can directly bind to actins and lipid membranes (8, 27, 74), though the roles of such interactions in axons have not been investigated. Additionally, ASAP1 may function through regulating the activity of ARF GTPases, which have been implicated in the regulation of membrane trafficking (75–77) and cytoskeletal remodeling (78, 79). The reported ASAP1-SH3 domain binding partners such as APC, FAK1, PYK2, and paxillin as well as Clasp1/2, β-Pix, and Limk1 identified in this study all exist in axons (80–87), and they are all known to regulate actin and/or microtubule structures, suggesting a role of ASAP1 in organizing these cytoskeletal regulatory proteins in axons, contributing to axon development and functions, which is an attractive direction for future studies.

Roles of ASAP1 in invadosomes and cancer metastasis

Cell invasion occurs in both physiological and pathological processes, such as immune surveillance or cancer metastasis (88). Invadosomes, encompassing podosomes, and invadopodia, serve as critical structures that mediate cell proteolytic invasion. ASAP1 bridges cortactin and paxillin with its proline-rich region and SH3 domain respectively, forming a tripartite complex that is indispensable for invadosome formation (5, 89). Moreover, many other ASAP1 binding proteins, including Arf6, Cin85, Src, FAK1, PYK2, and Limk1 are also known as necessary components of invadosomes, positioning ASAP1 as a key player in cell invasion processes (23, 47, 48, 90–94). On the other hand, ASAP1/ASAP2, together with some of their SH3 domain binder, like cortactin, paxillin,

and FAK1, have been strongly implicated in tumor invasion as well as malignancy, correlated with their highly upregulated expression in tumors and their direct involvements in invasive activities (2, 5, 16–23, 29, 95). Disruption of the cortactin-ASAP1-paxillin complex, either by overexpressing the ASAP1-SH3 domain or microinjection of peptides suppress ASAP1/cortactin interaction, has shown inhibitory effects on breast cancer cell invasion through matrigel (5, 17) or metastases formation in living animals (5). These observations supported the potential clinical values of the cell-penetrating peptide inhibiting ASAP1/2-SH3/target interaction in cancer metastasis developed in this study.

Experimental procedures

Constructs, protein expression, and purification

The coding sequences of the ASAP1 constructs were PCR amplified from a mouse brain coding DNA library. The coding sequences of AnkB constructs were PCR amplified from the full-length human 440-kD AnkB (a gift from Dr Vann Bennett, Duke University). Clasp1, Clasp2, and APC coding sequences were PCR amplified from mouse brain or human HEK293T complementary DNA libraries. All of the constructs used for protein expression were cloned onto a home-modified pET32a vector with or without a 3 × StrepII tag. All truncation mutations or point mutations were produced with the same strategy as described in our previous study (96). Protein expression and purification protocols are the same as previously described (96, 97). Recombinant proteins were expressed in BL21 (DE3) codon-plus *Escherichia coli* cells with induction by 0.1 mM IPTG at 16 °C. The N-terminal thioredoxin-His_6-tagged (Trx- His_6) proteins were purified using Ni^{2+}-NTA agarose affinity column followed by size-exclusion chromatography (Superdex 200 column from Cytiva) in the final buffer containing 50 mM Tris–HCl, pH 7.8, 1 mM DTT, and 1 mM EDTA, 100 mM NaCl. FITC-labeled peptides were chemically synthesized and checked with mass spectrum by ChinaPeptides (QYAOBIO) Co, Ltd.

Affinity purification and mass spectrum identification

The mouse brain specimens were obtained in accordance with the ethical review of laboratory animal welfare at Shenzhen Bay Laboratory. The brain tissue was immediately homogenized in a buffer solution consisting of 50 mM Hepes (pH 7.2), 600 mM NaCl, 15% glycerol, 0.1% Triton-X100, 20 mM CHAPS, 1 mM EDTA, 1 mM EGTA, 1 mM DTT, and a protease inhibitor cocktail (Cat. No. P8340, Sigma-Aldrich). The homogenates were then subjected to centrifugation at 90,000*g* for 40 min using an Ultracentrifuge (Optima XPN 100, Beckman Coulter). The resulting supernatant was dialyzed in a buffer solution containing 20 mM Hepes (pH 7.2), 200 mM NaCl, 5% glycerol, 1 mM EDTA, 1 mM EGTA, and 1 mM DTT, followed by another round of ultracentrifugation at 100,000*g* for 40 min. The protein concentration in the supernatant was determined using the Bradford assay, and the sample was prepared for the affinity purification.

For the affinity purification, the bait protein (gAnkB 1476–1727) was purified as a Trx-His_6-3 × StrepII tag fusion protein, and conjugated to the Strep-Tactin Sepharose beads (Cytiva). Brain lysate (1 ml for each sample) was firstly precleared by Strep-Tactin beads and then mixed with the bait protein conjugated beads (20 μl dry volume for 1 ml lysate), and incubated for 15 min, then centrifuged at 1000g for 1 min. The pellets containing the beads were washed three times with the dialysis buffer and then applied to SDS-PAGE. The SDS-PAGE gel was stained by Coomassie brilliant blue G-250, and protein bands were dissected for protein identification by mass spectrometry by Omicsolution Ltd.

Pull-down and western blot experiments

HEK293T cells transfected with Flag-tagged full-length ASAP1 plasmids were harvested 24 h posttransfection. Cells were lysed in a lysis buffer containing 50 mM Tris pH 7.5, 100 mM NaCl, 1 mM DTT, 1% Triton X-100, and protease inhibitors (Sigma-Aldrich Cat. NO. P8340). The supernatant was obtained by centrifugation at 15,000*g* for 10 min at 4 °C, and then diluted four-fold with PBS. Purified gAnkB 1476 to 1727 proteins (fused with Trx-His6-3 × StrepII tag) was added to the diluted supernatant and incubated for 30 min. Afterward, it was mixed with 20 μl of Strep-Tactin beads and incubated for 10 min at 4 °C, followed by three washes with PBS buffer. Finally, the beads with bound proteins were mixed with loading buffer and boiled at 100 °C for 5 min, and detected by Western blotting using a mouse monoclonal anti-Flag antibody (Sigma-Aldrich, Cat. NO. F3165). For pull-down experiments in Fig. S2, a similar method was used.

Isothermal titration calorimetry assay

ITC assays were carried out with the same protocol as described earlier using an ITC200 or a PEAQ-ITC MicroCal calorimeter (Malvern Panalytical) (96). Briefly, in each titration a purified protein was loaded into the syringe (at 300 μM, if not specified) and injected into the sample cell containing a binding partner (30 μM, if not specified). The reaction temperature was set to 25 °C, each experiment contained 19 titration points and the first titration point was discarded for data analysis. Data were analyzed and fitted using the programs provided by the manufacturer.

Crystallography

All crystals were obtained by sitting drop vapor diffusion methods at 16 °C. Crystals of gAnkB 1699 to 1710 in complex with ASAP1-SH3 were grown in solution containing 0.1 M Mes monohydrate, pH 6.0, 20% w/v polyethylene glycol 6000. Crystals were cryoprotected with 25% (v/v) glycerol and flash-cooled to 100 K. X-ray diffraction data were collected at the BL02U1 beamline of the Shanghai Synchrotron Radiation Facility. Data were processed and scaled using DIALS (98). Structures were solved by molecular replacement using PHASER (99), using the structure of the SH3E-DH unit of murine intersectin-1L (PDB: 3JV3) as the searching model. The model of AnkB peptide was manually built according to

Fo-Fc difference maps in COOT (100). Further model building and refinement were completed iteratively using COOT (100) and Refmac5 (101). The final models were validated by MolProbity (102) and statistics are summarized in Table 1. All structure figures were prepared by PyMOL (http://www.pymol.org).

Limk1 kinase phosphorylation assay

To evaluate the influence of SH3 protein on Limk1 kinase activity, a quantitative phosphorylation assay was conducted using the LIMK1 Kinase Enzyme System kit (Promega, Cat#VA7482) in accordance with the manufacturer's guidelines. Briefly, SH3 or Trx-strep proteins were prepared at specified concentrations in reaction buffer [40 mM Tris–HCl (pH 7.5), 20 mM $MgCl_2$ and 0.1 mg/ml bovine serum albumin (BSA), 50 μM DTT]. Subsequently, 1 μl of each protein solution was combined with 2 μl of Limk1 kinase solution and incubated for 10 min at room temperature to facilitate reaction. Three microliters of kinase samples were transferred to a 384-well plate and mixed with 2 μl of a 2.5 × ATP/Substrate (Native Swine Myelin Basic Protein) solution (250 μM ATP and 0.5 mg/ml Limk1 substrate). Following a brief centrifugation step at 4000*g* for 2 min, the kinase reactions were allowed to proceed for 60 min at room temperature. To terminate the reactions and initiate detection, 5 μl of ADP-Glo reagent was added to each well, followed by gentle mixing and a 60-min incubation at room temperature. This reagent depletes residual ATP, leaving only ADP for subsequent quantification. Next, 10 μl of kinase detection reagent was added to each well, followed by mixing and a final 60-min incubation at room temperature. This reagent generates a luminescent signal proportional to the amount of ADP present. Luminescence was measured using a BioTek plate-reading luminometer. The resulting data were then used to calculate the ATP conversion ratio for each reaction based on a previously generated ATP-to-ADP standard curve.

In vitro Limk1 phosphorylation assays were performed in reaction buffer containing 40 mM Tris (pH 7.5), 20 mM $MgCl_2$, 0.1 mg/ml BSA, 50 μM DTT, and 100 μM ATP at room temperature for 15 min or indicated times in the figures. Proteins were used as follows: Limk1 kinase domain 0.6 μM, ASAP1-SH3 (30 μM), MBP (0.5 mg/ml), and ASAP1-SH3 (30 μM) + MBP (0.5 mg/ml) if not specified. For time-dependent Limk1 autophosphorylation assay, 3 μM Limk1 kinase protein was used. For the Western blot of the phosphorylated proteins, the samples were applied to gradient SDS-PAGE gels and transferred to polyvinylidene fluoride membranes. After blocking for 1 h in 5% BSA, the membranes were incubated overnight at 4 °C with Phospho-Tyrosine antibody (Cell Signaling Technology, Cat. 8954S, Lot: 8), followed by secondary antibody staining for 1 h. Signals were detected with a Clarity Western ECL Substrate (Bio-Rad) by Amersham ImageQuant 800 machine and quantified using ImageJ software (https://fiji.sc/).

Transwell assay

Cell migration and invasion assays were performed in HeLa cells (From American Type Culture Collection, validated and tested free from *mycoplasma* contamination by sequencing) using Transwell chambers (Corning, #353097). For invasion assays, the upper chamber membranes were coated with Matrigel (Corning, #CLS354234), while membranes for migration assays were left uncoated. HeLa cells (3×10^4 cells/well) pretreated with the indicated cell-penetrating peptides for 24 h were seeded in serum-free medium within the upper chamber. A chemoattractant gradient was established by adding medium containing 20% fetal bovine serum to the lower chamber. Following a 24-h incubation period, the cells on the membrane were fixed with 4% paraformaldehyde and stained with crystal violet. Both non-migrated/invaded cells and migrated/invaded cells were imaged and quantified using ImageJ software.

Wound healing assay

To assess cell migration in a collective manner, a wound healing assay was used. HeLa cells (From American Type Culture Collection, validated and tested free from *mycoplasma* contamination by sequencing) pretreated with the indicated cell-penetrating peptides for 24 h, were seeded at a density of around 2.0×10^4 cells/well in the 2-well silicone insert (ibidi, #80209). After the formation of a confluent cell monolayer, the inserts were gently removed, creating a defined cell-free gap of approximately 500 ± 100 μm. The progression of wound closure was monitored and imaged at predetermined time intervals using an Olympus CKX53SF inverted microscope. ImageJ software was used to quantify the wound area at each time point, enabling the determination of the wound closure rate.

EdU assay

To evaluate cell proliferation, a 5-ethynyl-2′-deoxyuridine (EdU) incorporation assay was conducted. HeLa cells pretreated with indicated cell-penetrating peptides were seeded in glass-bottom cell culture dishes (Biosharp, #BS-15-GJM) and allowed to reach 70 to 80% confluence. Subsequently, the cells were incubated with 10 μM EdU working solution (Beyotime, #C0081S) for 2 h at 37 °C to enable EdU incorporation into newly synthesized DNA. Following the incubation period, cells were fixed with 4% paraformaldehyde, permeabilized with 0.3% Triton X-100 in PBS, and stained using the Click-iT EdU imaging kit according to the manufacturer's instructions. Hoechst 33342 was used to counterstain all nuclei. Images were acquired using a Zeiss LSM980 confocal microscope, and the percentage of EdU-positive cells, indicative of proliferating cells, was determined using ImageJ software.

Statistical analysis

Statistical analysis was conducted using GraphPad Prism 9.0 (https://www.graphpad.com/). Data are presented as the mean ± SD. When data assume Gaussian distribution confirmed by Shapiro–Wilk test, a two-tailed unpaired Student's *t* test was used to compare means between groups as specified. Otherwise, a Mann-Whitney test was conducted. $p < 0.05$ was considered significant. Each *p* value and the sample size are indicated in figure legends. Quantification of microscopy was performed using image J (Fiji; https://fiji.sc/).

Data availability

All data are contained within the manuscript. Further information and requests for resources and reagents including DNA constructs and recombinant proteins should be directed to Keyu Chen.

Supporting information—This article contains supporting information (62–68).

Acknowledgments—We thank the BL19U1 beamline at National Facility for Protein Science Shanghai (NFPS) for X-ray beam time.

Author contributions—Y. L., Y. Z., Y. H., F. L., and L. X., investigation; Y. L., K. L., and M. Z. writing–review and editing; Y. L. and K. C. formal analysis; Y. L. methodology; K. L. and M. Z. supervision; M. Z. and K. C. conceptualization; M. Z. and K. C. funding acquisition; K. C. writing–original draft.

Funding and additional information—This work was supported by a grant from the National Nature Science Foundation of China (32000874), grants from the Shenzhen Bay laboratory (S201101002, 21320011, and QH32001), and grants from Shenzhen Government (ZDSYS20220402111000001 and JCYJ20220818100215033).

Conflict of interest—The authors declare that they have no conflicts of interest with the contents of this article.

Abbreviations—The abbreviations used are: BSA, bovine serum albumin; EdU, 5-ethynyl-2′-deoxyuridine; gAnkB, giant ankyrin-B; ITC, isothermal titration calorimetry; MBP, myelin basic protein; PDB, Protein Data Bank; PH, pleckstrin homology.

References

1. Furman, C., Short, S. M., Subramanian, R. R., Zetter, B. R., and Roberts, T. M. (2002) DEF-1/ASAP1 is a GTPase-activating protein (GAP) for ARF1 that enhances cell motility through a GAP-dependent mechanism. *J. Biol. Chem.* **277**, 7962–7969
2. Brown, M. T., Andrade, J., Radhakrishna, H., Donaldson, J. G., Cooper, J. A., and Randazzo, P. A. (1998) ASAP1, a phospholipid-dependent Arf GTPase-activating protein that associates with and is phosphorylated by src. *Mol. Cell. Biol.* **18**, 7038–7051
3. Liu, Y., Loijens, J. C., Martin, K. H., Karginov, A. V., and Parsons, J. T. (2002) The association of ASAP1, an ADP ribosylation factor-GTPase activating protein, with focal adhesion kinase contributes to the process of focal adhesion assembly. *Mol. Biol. Cell.* **13**, 2147–2156
4. Liu, Y., Yerushalmi, G. M., Grigera, P. R., and Parsons, J. T. (2005) Mislocalization or reduced expression of Arf GTPase-activating protein ASAP1 inhibits cell spreading and migration by influencing Arf1 GTPase cycling *. *J. Biol. Chem.* **280**, 8884–8892
5. Onodera, Y., Hashimoto, S., Hashimoto, A., Morishige, M., Mazaki, Y., Yamada, A., *et al.* (2005) Expression of AMAP1, an ArfGAP, provides novel targets to inhibit breast cancer invasive activities. *EMBO J.* **24**, 963–973
6. Randazzo, P. A., Andrade, J., Miura, K., Brown, M. T., Long, Y.-Q., Stauffer, S., *et al.* (2000) The Arf GTPase-activating protein ASAP1 regulates the actin cytoskeleton. *Proc. Natl. Acad. Sci.* **97**, 4011–4016
7. Bharti, S., Inoue, H., Bharti, K., Hirsch, D. S., Nie, Z., Yoon, H.-Y., *et al.* (2007) Src-dependent phosphorylation of ASAP1 regulates podosomes. *Mol. Cell. Biol.* **27**, 8271–8283
8. Chen, P.-W., Billington, N., Maron, B. Y., Sload, J. A., Chinthalapudi, K., and Heissler, S. M. (2020) The BAR domain of the Arf GTPase-activating protein ASAP1 directly binds actin filaments. *J. Biol. Chem.* **295**, 11303–11315
9. Curtis, J., Luo, Y., Zenner, H. L., Cuchet-Lourenço, D., Wu, C., Lo, K., *et al.* (2015) Susceptibility to tuberculosis is associated with variants in the ASAP1 gene encoding a regulator of dendritic cell migration. *Nat. Genet.* **47**, 523–527
10. Shiba, Y., and Randazzo, P. A. (2011) GEFH1 binds ASAP1 and regulates podosome formation. *Biochem. Biophys. Res. Commun.* **406**, 574–579
11. Oda, A., Wada, I., Miura, K., Okawa, K., Kadoya, T., Kato, T., *et al.* (2003) CrkL directs ASAP1 to peripheral focal adhesions. *J. Biol. Chem.* **278**, 6456–6460
12. Gasilina, A., Vitali, T., Luo, R., Jian, X., and Randazzo, P. A. (2019) The ArfGAP ASAP1 controls actin stress fiber organization via its N-BAR domain. *iScience* **22**, 166–180
13. Buffart, T. E., Coffa, J., Hermsen, M. A. J. A., Carvalho, B., van der Sijp, J. R. M., Ylstra, B., *et al.* (2005) DNA copy number changes at 8q11-24 in metastasized colorectal cancer. *Cell. Oncol.* **27**, 57–65
14. Chen, P.-W., Jian, X., Heissler, S. M., Le, K., Luo, R., Jenkins, L. M., *et al.* (2016) The Arf GTPase-activating protein, ASAP1, binds nonmuscle myosin 2A to control remodeling of the actomyosin network. *J. Biol. Chem.* **291**, 7517–7526
15. Martin, R. K., and Jackson, T. R. (2005) Centaurin β4 in cancer. *Biochem. Soc. Trans.* **33**, 1282–1284
16. Hashimoto, S., Furukawa, S., Hashimoto, A., Tsutaho, A., Fukao, A., Sakamura, Y., *et al.* (2019) ARF6 and AMAP1 are major targets of KRAS and TP53 mutations to promote invasion, PD-L1 dynamics, and immune evasion of pancreatic cancer. *Proc. Natl. Acad. Sci.* **116**, 17450–17459
17. Hashimoto, S., Hirose, M., Hashimoto, A., Morishige, M., Yamada, A., Hosaka, H., *et al.* (2006) Targeting AMAP1 and cortactin binding bearing an atypical src homology 3/proline interface for prevention of breast cancer invasion and metastasis. *Proc. Natl. Acad. Sci.* **103**, 7036–7041
18. Müller, T., Stein, U., Poletti, A., Garzia, L., Rothley, M., Plaumann, D., *et al.* (2010) ASAP1 promotes tumor cell motility and invasiveness, stimulates metastasis formation in vivo, and correlates with poor survival in colorectal cancer patients. *Oncogene* **29**, 2393–2403
19. Fujii, A., Masuda, T., Iwata, M., Tobo, T., Wakiyama, H., Koike, K., *et al.* (2021) The novel driver gene ASAP2 is a potential druggable target in pancreatic cancer. *Cancer Sci.* **112**, 1655–1668
20. Lin, D., Watahiki, A., Bayani, J., Zhang, F., Liu, L., Ling, V., *et al.* (2008) ASAP1, a gene at 8q24, is associated with prostate cancer metastasis. *Cancer Res.* **68**, 4352–4359
21. Sabe, H., Hashimoto, S., Morishige, M., Ogawa, E., Hashimoto, A., Nam, J.-M., *et al.* (2009) The EGFR-GEP100-Arf6-AMAP1 signaling pathway specific to breast cancer invasion and metastasis. *Traffic* **10**, 982–993
22. Onodera, Y., Nam, J.-M., Hashimoto, A., Norman, J. C., Shirato, H., Hashimoto, S., *et al.* (2012) Rab5c promotes AMAP1-PRKD2 complex formation to enhance β1 integrin recycling in EGF-induced cancer invasion. *J. Cell Biol.* **197**, 983–996
23. Nam, J., Onodera, Y., Mazaki, Y., Miyoshi, H., Hashimoto, S., and Sabe, H. (2007) CIN85, a Cbl-interacting protein, is a component of AMAP1-mediated breast cancer invasion machinery. *EMBO J.* **26**, 647–656
24. Schreiber, C., Saraswati, S., Harkins, S., Gruber, A., Cremers, N., Thiele, W., *et al.* (2019) Loss of ASAP1 in mice impairs adipogenic and osteogenic differentiation of mesenchymal progenitor cells through dysregulation of FAK/Src and AKT signaling. *PLoS Genet.* **15**, e1008216
25. Jian, X., Brown, P., Schuck, P., Gruschus, J. M., Balbo, A., Hinshaw, J. E., *et al.* (2009) Autoinhibition of Arf GTPase-activating protein activity by the BAR domain in ASAP1. *J. Biol. Chem.* **284**, 1652–1663
26. Luo, R., Miller Jenkins, L. M., Randazzo, P. A., and Gruschus, J. (2008) Dynamic interaction between Arf GAP and PH domains of ASAP1 in the regulation of GAP activity. *Cell. Signal.* **20**, 1968–1977
27. Soubias, O., Pant, S., Heinrich, F., Zhang, Y., Roy, N. S., Li, J., *et al.* (2020) Membrane surface recognition by the ASAP1 PH domain and consequences for interactions with the small GTPase Arf1. *Sci. Adv.* **6**, eabd1882
28. Kowanetz, K., Husnjak, K., Höller, D., Kowanetz, M., Soubeyran, P., Hirsch, D., *et al.* (2004) CIN85 associates with multiple effectors controlling intracellular trafficking of epidermal growth factor receptors. *Mol. Biol. Cell.* **15**, 3155–3166

29. Luo, Q., Zhang, S., Zhang, D., Yuan, F., Chen, X., and Yang, S. (2020) Expression of ASAP1 and FAK in gastric cancer and its clinicopathological significance. *Oncol. Lett.* **20**, 974–980
30. Kruljac-Letunic, A., Moelleken, J., Kallin, A., Wieland, F., and Blaukat, A. (2003) The tyrosine kinase Pyk2 regulates Arf1 activity by phosphorylation and inhibition of the Arf-GTPase-activating protein ASAP1. *J. Biol. Chem.* **278**, 29560–29570
31. Oshiro, T., Koyama, S., Sugiyama, S., Kondo, A., Onodera, Y., Asahara, T., *et al.* (2002) Interaction of POB1, a downstream molecule of small G protein ral, with PAG2, a paxillin-binding protein, is involved in cell migration. *J. Biol. Chem.* **277**, 38618–38626
32. Kaneko, T., Li, L., and Li, S. S.-C. (2008) The SH3 domain–a family of versatile peptide- and protein-recognition module. *Front. Biosci. J. Virtual Libr.* **13**, 4938–4952
33. Li, S. S.-C. (2005) Specificity and versatility of SH3 and other proline-recognition domains: structural basis and implications for cellular signal transduction. *Biochem. J.* **390**, 641–653
34. Dionne, U., Chartier, F. J. M., López de Los Santos, Y., Lavoie, N., Bernard, D. N., Banerjee, S. L., *et al.* (2018) Direct phosphorylation of SRC homology 3 domains by tyrosine kinase receptors disassembles ligand-induced signaling networks. *Mol. Cell.* **70**, 995–1007.e11
35. Teyra, J., Huang, H., Jain, S., Guan, X., Dong, A., Liu, Y., *et al.* (2017) Comprehensive analysis of the human SH3 domain family reveals a wide variety of non-canonical specificities. *Struct. Lond. Engl. 1993* **25**, 1598–1610.e3
36. Vogel, C., and Chothia, C. (2006) Protein family expansions and biological complexity. *Plos Comput. Biol.* **2**, e48
37. Xin, X., Gfeller, D., Cheng, J., Tonikian, R., Sun, L., Guo, A., *et al.* (2013) SH3 interactome conserves general function over specific form. *Mol. Syst. Biol.* **9**, 652
38. Feng, S., Kasahara, C., Rickles, R. J., and Schreiber, S. L. (1995) Specific interactions outside the proline-rich core of two classes of Src homology 3 ligands. *Proc. Natl. Acad. Sci.* **92**, 12408–12415
39. Lim, W. A., Richards, F. M., and Fox, R. O. (1994) Structural determinants of peptide-binding orientation and of sequence specificity in SH3 domains. *Nature* **372**, 375–379
40. Saksela, K., and Permi, P. (2012) SH3 domain ligand binding: what's the consensus and where's the specificity? *FEBS Lett.* **586**, 2609–2614
41. Yu, H., Chen, J. K., Feng, S., Dalgarno, D. C., Brauer, A. W., and Schrelber, S. L. (1994) Structural basis for the binding of proline-rich peptides to SH3 domains. *Cell.* **76**, 933–945
42. Bennett, V., and Walder, K. (2015) Evolution in action: giant ankyrins awake. *Dev. Cell.* **33**, 1–2
43. Yang, R., Walder-Christensen, K. K., Kim, N., Wu, D., Lorenzo, D. N., Badea, A., *et al.* (2019) ANK2 autism mutation targeting giant ankyrin-B promotes axon branching and ectopic connectivity. *Proc. Natl. Acad. Sci.* **116**, 15262–15271
44. Chen, K., Yang, R., Li, Y., Zhou, J. C., and Zhang, M. (2020) Giant ankyrin-B suppresses stochastic collateral axon branching through direct interaction with microtubules. *J. Cell Biol.* **219**, 201910053
45. Jia, X., Lin, L., Xu, S., Li, L., Wei, Z., Yu, C., *et al.* (2023) Crystal structure of the SH3 domain of ASAP1 in complex with the proline rich motif (PRM) of MICAL1 reveals a unique SH3/PRM interaction mode. *Int. J. Mol. Sci.* **24**, 1414
46. Matsui, C., Kaieda, S., Ikegami, T., and Mimori-Kiyosue, Y. (2008) Identification of a link between the SAMP repeats of adenomatous polyposis coli tumor suppressor and the src homology 3 domain of DDEF. *J. Biol. Chem.* **283**, 33006–33020
47. Lagoutte, E., Villeneuve, C., Lafanechère, L., Wells, C. M., Jones, G. E., Chavrier, P., *et al.* (2016) LIMK regulates tumor-cell invasion and matrix degradation through tyrosine phosphorylation of MT1-MMP. *Sci. Rep.* **6**, 24925
48. Mak, A. S. (2014) p53 in cell invasion, podosomes, and invadopodia. *Cell Adhes. Migr.* **8**, 205–214
49. Okano, I., Hiraoka, J., Otera, H., Nunoue, K., Ohashi, K., Iwashita, S., *et al.* (1995) Identification and characterization of a novel family of serine/threonine kinases containing two N-terminal LIM motifs. *J. Biol. Chem.* **270**, 31321–31330
50. Engel, U., Zhan, Y., Long, J. B., Boyle, S. N., Ballif, B. A., Dorey, K., *et al.* (2014) Abelson phosphorylation of CLASP2 modulates its association with microtubules and actin. *Cytoskelet. Hoboken NJ* **71**, 195–209
51. Lee, H., Engel, U., Rusch, J., Scherrer, S., Sheard, K., and Van Vactor, D. (2004) The microtubule plus end tracking protein Orbit/MAST/CLASP acts downstream of the tyrosine kinase Abl in mediating axon guidance. *Neuron* **42**, 913–926
52. Di Martino, J., Paysan, L., Gest, C., Lagrée, V., Juin, A., Saltel, F., *et al.* (2014) Cdc42 and Tks5: a minimal and universal molecular signature for functional invadosomes. *Cell Adhes. Migr.* **8**, 280–292
53. Wu, X., Gan, B., Yoo, Y., and Guan, J.-L. (2005) FAK-mediated src phosphorylation of endophilin A2 inhibits endocytosis of MT1-MMP and promotes ECM degradation. *Dev. Cell.* **9**, 185–196
54. Destaing, O., Sanjay, A., Itzstein, C., Horne, W. C., Toomre, D., De Camilli, P., *et al.* (2008) The tyrosine kinase activity of c-Src regulates actin dynamics and organization of podosomes in osteoclasts. *Mol. Biol. Cell.* **19**, 394–404
55. Mehrabipour, M., Jasemi, N. S. K., Dvorsky, R., and Ahmadian, M. R. (2023) A systematic compilation of human SH3 domains: a versatile superfamily in cellular signaling. *Cells* **12**, 2054
56. Kazemein Jasemi, N. S., Mehrabipour, M., Magdalena Estirado, E., Brunsveld, L., Dvorsky, R., and Ahmadian, M. R. (2024) Functional classification and interaction selectivity landscape of the human SH3 domain superfamily. *Cells* **13**, 195
57. Guidotti, G., Brambilla, L., and Rossi, D. (2017) Cell-penetrating peptides: from basic research to clinics. *Trends Pharmacol. Sci.* **38**, 406–424
58. Nadal-Bufí, F., and Henriques, S. T. (2020) How to overcome endosomal entrapment of cell-penetrating peptides to release the therapeutic potential of peptides? *Pept. Sci.* **112**, e24168
59. Lönn, P., Kacsinta, A. D., Cui, X.-S., Hamil, A. S., Kaulich, M., Gogoi, K., *et al.* (2016) Enhancing endosomal escape for intracellular delivery of macromolecular biologic therapeutics. *Sci. Rep.* **6**, 32301
60. Li, M., Tao, Y., Shu, Y., LaRochelle, J. R., Steinauer, A., Thompson, D., *et al.* (2015) Discovery and characterization of a peptide that enhances endosomal escape of delivered proteins in vitro and in vivo. *J. Am. Chem. Soc.* **137**, 14084–14093
61. Voltà-Durán, E., Parladé, E., Serna, N., Villaverde, A., Vazquez, E., and Unzueta, U. (2023) Endosomal escape for cell-targeted proteins. Going out after going in. *Biotechnol. Adv.* **63**, 108103
62. Gorelik, M., and Davidson, A. R. (2012) Distinct peptide binding specificities of Src homology 3 (SH3) protein domains can be determined by modulation of local energetics across the binding interface. *J. Biol. Chem.* **287**, 9168–9177
63. Grabs, D., Slepnev, V. I., Songyang, Z., David, C., Lynch, M., Cantley, L. C., *et al.* (1997) The SH3 domain of amphiphysin binds the proline-rich domain of dynamin at a single site that defines a new SH3 binding consensus sequence. *J. Biol. Chem.* **272**, 13419–13425
64. Harkiolaki, M., Lewitzky, M., Gilbert, R. J. C., Jones, E. Y., Bourette, R. P., Mouchiroud, G., *et al.* (2003) Structural basis for SH3 domain-mediated high-affinity binding between Mona/Gads and SLP-76. *EMBO J.* **22**, 2571–2582
65. Seet, B. T., Berry, D. M., Maltzman, J. S., Shabason, J., Raina, M., Koretzky, G. A., *et al.* (2007) Efficient T-cell receptor signaling requires a high-affinity interaction between the Gads C-SH3 domain and the SLP-76 RxxK motif. *EMBO J.* **26**, 678–689
66. Desrochers, G., Cappadocia, L., Lussier-Price, M., Ton, A.-T., Ayoubi, R., Serohijos, A., *et al.* (2017) Molecular basis of interactions between SH3 domain-containing proteins and the proline-rich region of the ubiquitin ligase Itch. *J. Biol. Chem.* **292**, 6325–6338
67. Desrochers, G., Lussier-Price, M., Omichinski, J. G., and Angers, A. (2015) Multiple src homology 3 binding to the ubiquitin ligase itch conserved proline-rich region. *Biochemistry* **54**, 7345–7354
68. Kami, K., Takeya, R., Sumimoto, H., and Kohda, D. (2002) Diverse recognition of non-PxxP peptide ligands by the SH3 domains from p67(phox), Grb2 and Pex13p. *EMBO J.* **21**, 4268–4276
69. Leterrier, C., Dubey, P., and Roy, S. (2017) The nano-architecture of the axonal cytoskeleton. *Nat. Rev. Neurosci.* **18**, 713–726

70. Sousa, S. C., and Sousa, M. M. (2021) The cytoskeleton as a modulator of tension driven axon elongation. *Dev. Neurobiol.* **81**, 300–309
71. Zhang, C., and Rasband, M. N. (2016) Cytoskeletal control of axon domain assembly and function. *Curr. Opin. Neurobiol.* **39**, 116–121
72. De Rubeis, S., He, X., Goldberg, A. P., Poultney, C. S., Samocha, K., Ercument Cicek, A., *et al.* (2014) Synaptic, transcriptional and chromatin genes disrupted in autism. *Nature* **515**, 209–215
73. Iossifov, I., O'Roak, B. J., Sanders, S. J., Ronemus, M., Krumm, N., Levy, D., *et al.* (2014) The contribution of de novo coding mutations to autism spectrum disorder. *Nature* **515**, 216–221
74. Che, M. M., Boja, E. S., Yoon, H.-Y., Gruschus, J., Jaffe, H., Stauffer, S., *et al.* (2005) Regulation of ASAP1 by phospholipids is dependent on the interface between the PH and Arf GAP domains. *Cell. Signal.* **17**, 1276–1288
75. Mima, J. (2021) Self-assemblies of Rab- and Arf-family small GTPases on lipid bilayers in membrane tethering. *Biophys. Rev.* **13**, 531–539
76. Mizuno-Yamasaki, E., Rivera-Molina, F., and Novick, P. (2012) GTPase networks in membrane traffic. *Annu. Rev. Biochem.* **81**, 637–659
77. Nawrotek, A., Zeghouf, M., and Cherfils, J. (2020) Protein-membrane interactions in small GTPase signalling and pharmacology: perspectives from Arf GTPases studies. *Biochem. Soc. Trans.* **48**, 2721–2728
78. Singh, V., Davidson, A. C., Hume, P. J., Humphreys, D., and Koronakis, V. (2019) Arf GTPase interplay with Rho GTPases in regulation of the actin cytoskeleton. *Small GTPases* **10**, 411–418
79. Tanna, C. E., Goss, L. B., Ludwig, C. G., and Chen, P.-W. (2019) Arf GAPs as regulators of the actin cytoskeleton-an update. *Int. J. Mol. Sci.* **20**, 442
80. Mao, R., Deng, R., Wei, Y., Han, L., Meng, Y., Xie, W., *et al.* (2019) LIMK1 and LIMK2 regulate cortical development through affecting neural progenitor cell proliferation and migration. *Mol. Brain* **12**, 67
81. Rico, B., Beggs, H. E., Schahin-Reed, D., Kimes, N., Schmidt, A., and Reichardt, L. F. (2004) Control of axonal branching and synapse formation by focal adhesion kinase. *Nat. Neurosci.* **7**, 1059–1069
82. López Tobón, A., Suresh, M., Jin, J., Vitriolo, A., Pietralla, T., Tedford, K., *et al.* (2018) The guanine nucleotide exchange factor Arhgef7/βPix promotes axon formation upstream of TC10. *Sci. Rep.* **8**, 8811
83. Sayas, C. L., Basu, S., van der Reijden, M., Bustos-Morán, E., Liz, M., Sousa, M., *et al.* (2019) Distinct functions for mammalian CLASP1 and -2 during neurite and axon elongation. *Front. Cell. Neurosci.* **13**, 5
84. Menegon, A., Burgaya, F., Baudot, P., Dunlap, D. D., Girault, J. A., and Valtorta, F. (1999) FAK+ and PYK2/CAKbeta, two related tyrosine kinases highly expressed in the central nervous system: similarities and differences in the expression pattern. *Eur. J. Neurosci.* **11**, 3777–3788
85. Robles, E., and Gomez, T. M. (2006) Focal adhesion kinase signaling at sites of integrin-mediated adhesion controls axon pathfinding. *Nat. Neurosci.* **9**, 1274–1283
86. Li, C., and Götz, J. (2018) Pyk2 is a novel tau tyrosine kinase that is regulated by the tyrosine kinase fyn. *J. Alzheimers Dis. JAD.* **64**, 205–221
87. Shi, S.-H., Cheng, T., Jan, L. Y., and Jan, Y.-N. (2004) APC and GSK-3beta are involved in mPar3 targeting to the nascent axon and establishment of neuronal polarity. *Curr. Biol. CB.* **14**, 2025–2032
88. Linder, S., Cervero, P., Eddy, R., and Condeelis, J. (2023) Mechanisms and roles of podosomes and invadopodia. *Nat. Rev. Mol. Cell Biol.* **24**, 86–106
89. Bowden, E. T., Barth, M., Thomas, D., Glazer, R. I., and Mueller, S. C. (1999) An invasion-related complex of cortactin, paxillin and PKCμ associates with invadopodia at sites of extracellular matrix degradation. *Oncogene* **18**, 4440–4449
90. Heckel, T., Czupalla, C., Expirto Santo, A. I., Anitei, M., Arantzazu Sanchez-Fernandez, M., Mosch, K., *et al.* (2009) Src-dependent repression of ARF6 is required to maintain podosome-rich sealing zones in bone-digesting osteoclasts. *Proc. Natl. Acad. Sci. U. S. A.* **106**, 1451–1456
91. Schramp, M., Ying, O., Kim, T. Y., and Martin, G. S. (2008) ERK5 promotes Src-induced podosome formation by limiting Rho activation. *J. Cell Biol.* **181**, 1195–1210
92. Pan, Y.-R., Chen, C.-L., and Chen, H.-C. (2011) FAK is required for the assembly of podosome rosettes. *J. Cell Biol.* **195**, 113–129
93. Gil-Henn, H., Destaing, O., Sims, N. A., Aoki, K., Alles, N., Neff, L., *et al.* (2007) Defective microtubule-dependent podosome organization in osteoclasts leads to increased bone density in Pyk2(-/-) mice. *J. Cell Biol.* **178**, 1053–1064
94. Genna, A., Lapetina, S., Lukic, N., Twafra, S., Meirson, T., Sharma, V. P., *et al.* (2018) Pyk2 and FAK differentially regulate invadopodia formation and function in breast cancer cells. *J. Cell Biol.* **217**, 375–395
95. Sabe, H., Onodera, Y., Mazaki, Y., and Hashimoto, S. (2006) ArfGAP family proteins in cell adhesion, migration and tumor invasion. *Curr. Opin. Cell Biol.* **18**, 558–564
96. Chen, K., Li, J., Wang, C., Wei, Z., and Zhang, M. (2017) Autoinhibition of ankyrin-B/G membrane target bindings by intrinsically disordered segments from the tail regions. *eLife* **6**, e29150
97. Li, J., Chen, K., Zhu, R., and Zhang, M. (2020) Structural basis underlying strong interactions between ankyrins and spectrins. *J. Mol. Biol.* **432**, 3838–3850
98. Gildea, R. J., Beilsten-Edmands, J., Axford, D., Horrell, S., Aller, P., Sandy, J., *et al.* (2022) xia2.multiplex: a multi-crystal data-analysis pipeline. *Acta Crystallogr. Sect. Struct. Biol.* **78**, 752–769
99. McCoy, A. J., Grosse-Kunstleve, R. W., Adams, P. D., Winn, M. D., Storoni, L. C., and Read, R. J. (2007) Phaser crystallographic software. *J. Appl. Crystallogr.* **40**, 658–674
100. Emsley, P., Lohkamp, B., Scott, W. G., and Cowtan, K. (2010) Features and development of coot. *Acta Crystallogr. D Biol. Crystallogr.* **66**, 486–501
101. Murshudov, G. N., Skubák, P., Lebedev, A. A., Pannu, N. S., Steiner, R. A., Nicholls, R. A., *et al.* (2011) REFMAC5 for the refinement of macromolecular crystal structures. *Acta Crystallogr. D Biol. Crystallogr.* **67**, 355–367
102. Chen, V. B., Arendall, W. B., Headd, J. J., Keedy, D. A., Immormino, R. M., Kapral, G. J., *et al.* (2010) MolProbity: all-atom structure validation for macromolecular crystallography. *Acta Crystallogr. D Biol. Crystallogr.* **66**, 12–21